

RESEARCH ARTICLE

10.1029/2020JF005663

Key Points:

- Hypogenic and epigenic evolution is considered for deep underwater caves
- Geophysical models show geometry and extent of the Hranice Abyss
- A new formation model of the Hranice Abyss based on epigenic formation is presented

Correspondence to:

R. Klanica,
rk@ig.cas.cz

Citation:

Klanica, R., Kadlec, J., Tábořík, P., Mrlina, J., Valenta, J., & Kováčiková, S., et al. (2020). Hypogenic versus epigenic origin of deep underwater caves illustrated by the Hranice Abyss (Czech Republic)—The world's deepest freshwater cave. *Journal of Geophysical Research: Earth Surface*, 125, e2020JF005663. <https://doi.org/10.1029/2020JF005663>

Received 17 APR 2020

Accepted 10 AUG 2020

Accepted article online 15 JUL 2020

Hypogenic Versus Epigenic Origin of Deep Underwater Caves Illustrated by the Hranice Abyss (Czech Republic)—The World's Deepest Freshwater Cave

Radek Klanica¹ , Jaroslav Kadlec¹ , Petr Tábořík^{2,3} , Jan Mrlina¹ , Jan Valenta² , Světlana Kováčiková¹ , and Graham J. Hill¹ 

¹Institute of Geophysics, Czech Academy of Sciences, Prague, Czech Republic, ²Faculty of Science, Institute of Hydrogeology, Engineering Geology and Applied Geophysics, Charles University, Prague, Czech Republic, ³Institute of Rock Structure and Mechanics, Czech Academy of Sciences, Prague, Czech Republic

Abstract Extremely deep freshwater filled cave systems are common in karst systems globally. The origin and evolution of such caves are usually attributed to hypogenic (bottom-up) processes, in which acidic groundwater dissolves limestone from below. However, these deep cave systems can form by epigenic (top-down) processes, with meteoric waters descending from the surface underground. The Hranice Abyss (Czech Republic), with a reached depth of 473.5 m, is the deepest mapped extent of such a system globally, although its maximum depth is unknown. Multiple geophysical data sets (gravity, electrical resistivity tomography, audiomagnetotellurics, and seismic refraction and reflection) are used to investigate the extent and formation of the Hranice Abyss. The geophysical results suggest the Hranice Abyss extends to depths of ~1 km. Further, we identify structures within the karst, including buried cockpit karst towers with several NW-SE-oriented valleys. The new geophysical results from the Hranice Abyss, considered in combination with geological constraints of the region (tectonic evolution and morphology of karst structure), suggest an epigenic formation process, rather than the traditionally invoked hypogenic origin. Formation by epigenic rather than hypogenic processes has implications for local and regional karst history associated with areas hosting deep karst systems.

1. Introduction

Whether large cave systems formed via epigenic or hypogenic processes is a fundamental question for understanding the regional and local karst processes of the cave area. Epigenic caves form by top-down dissolution of meteoric water enriched with soil CO₂ infiltrating from the surface and may be the dominant formation processes for as many as 80–90% of known caves (Audra & Palmer, 2015). On the other hand, hypogenic cave systems form from a bottom-up migration of deep-sourced thermally elevated CO₂-H₂S bearing fluids, often typically related to volcanic/mantle structures (Klimchouk et al., 2017) or more rarely to petroleum generating processes (DuChene et al., 2017). Hypogenic fluids in the upper crust result in groundwater enriched with strong acids (e.g., CO₂, H₂S, or HCl) that can upwell via artesian aquifers or interformational flow in/from the zone of fluid-geodynamic influence along faults or fractured zones (Klimchouk et al., 2017).

Determining the evolution dominant process and formation history of deep-flooded cave systems is complicated by the difficulty of completing detailed exploration beneath the water table. Flooded deep karst cave systems are found globally (Vysoká et al., 2019) for example, in Italy (Pozzo del Merro, 392 m), Mexico (Zacatón, 335 m), Brazil (Lagoa Misteriosa, 220 m), and South Africa (Boesmansgat, 283 m). The commonly invoked mechanism of formation of these vertical caves is hypogenic (Klimchouk et al., 2017), largely based on present-day observations such as groundwater filling the Pozzo del Merro and El Zacatón abysses being enriched by CO₂ and H₂S from nearby volcanic centers (Gary, 2017; Gary et al., 2003).

The local structure of karstified regions is a controlling factor in the formation of horizontal or vertical cave morphologies. Further, the surficial geomorphic evolution (e.g., variations in the erosional base elevation) of the surrounding landscape also plays a fundamental role in the evolution of epigenic cave systems (Ford & Williams, 2007). Deep epigenic water-filled caves have developed in southern France (Fontaine de Vaucluse, 308 m; Audra et al., 2004) and in Croatia (Red Lake, 350 m; Andrić & Bonacci, 2014). The

formation of Fountaine de Vaucluse was triggered by a dramatic regional erosional base elevation decrease during the Messinian period (5.96–5.32 Ma) when the Mediterranean Sea was almost dry. The erosional base drop quickly led to river valley deepening, followed by the formation of a deep cave system. Marine transgression caused the end of the Messinian lowstand, which led the deep canyon-like valleys in the karst regions to be infilled with clastic sequences. The pre-Messinian freshwater springs flowing at the base of the canyon system did not experience a corresponding rise in base level associated with the canyon filling sedimentation; rather, they became “buried,” leading to bottom-up flooding of the karst cave systems (Audra et al., 2004).

The Hranice Abyss (HA) currently represents the deepest flooded freshwater cave in the world, with a maximum depth 473.5 m below surface estimated using a ROV (remote-operated vehicle). The depth the submersible reached was limited by the length of the fiber-optic communication cable and, as such, does not represent the full extent of the cave system (Guba, 2016; Zajiček, 2020). The HA is filled with Ca-HCO₃ mineral water enriched by CO₂ with temperature varying from 14.5–18.8°C depending on seasonal variations and the depth below the water table level (Vysoká et al., 2019). Stable isotopic CO₂ compositions, together with a ratio of ³He/⁴He dissolved in the water, indicate an origin of the gasses close to the Earth’s mantle/crust transition (e.g., Meyberg & Rinne, 1995; Šmejkal et al., 1976; Sracek et al., 2019), evoking the possibility of the extreme depth of the HA (Meyberg & Rinne, 1995) and suggesting a hypogene (hydrothermal) origin of the HA (e.g., Sracek et al., 2019; Zajiček, 2020), following an early accepted view on the Hranice Karst area evolution (Hynie & Kodým, 1936).

Geophysical methods have been frequently used to image subsurface karst structure (e.g., Carvalho et al., 2005; Zhou et al., 2002). Geophysical imaging of these regions can provide valuable information needed for reconstruction of the tectonic and morphological evolution of these areas. In the case of cave formation features, such as a well-developed and deep-seated fault network, and alteration zones resulting from large-scale fluxing of heated waters and mantle-derived gasses are indicative of hypogenic formation, while a complex shallow drainage pattern morphology, including sinkholes and dolines, suggests epigenetic formation.

We use the results from geophysical surveys of the HA area to reveal the local geological and morphological structures within the HA. The new geophysical results are then integrated with regional tectonic history and period of formation of the HA in a reassessment of its formation mechanism. A similar approach may be applied to other deep-flooded karst cave systems globally to identify the key karst structures associated with each of the formation mechanisms.

2. Geological Settings and Karst Evolution

The HA is a part of the Hranice Karst (HK) located in the eastern part of the Czech Republic, ~35 km east of Olomouc City. The HK covers an ~15 km² area and formed at a contact between the Bohemian Massif and Outer Western Carpathians within the Carpathian orogenic belt. The carbonate rocks, susceptible to karst processes, were deposited on carbonate platforms and reef slopes in a tropical ocean during the Middle Devonian and Early Carboniferous (Macocho and Líšeň Fms.) (Otava, 2010). The estimated thickness of carbonates reaches 1.2 km based on a coring conducted about 11 km SE of the HK area (Sracek et al., 2019). Deposition of overlying Carboniferous turbidite flysch sequences, up to 6 km thick, indicate deepening of the sedimentary basin (Bubík et al., 2018). Both carbonate and clastic sequences were folded and thrust during the Variscan Orogeny in the Late Carboniferous (Kalvoda et al., 2008). In the Carpathian domain, marine siliciclastic and flysch sediments were deposited within the Cretaceous and Paleogene periods. These sequences were folded and thrust over the eastern margin of the Bohemian Massif during the Alpine Orogeny since the Oligocene/Miocene transition to the mid-Miocene (early Langhian). The frontal thrust terminations are found very close to the HK area (Figure 1). Parallel with the Carpathian deformation front, the Carpathian Foredeep (CF) basin originated during the early Miocene (Burdigalian) and subsequently was filled with shallow-water carbonates and marine clastic deposits (e.g., Sracek et al., 2019). The CF segment passing along the HK area was opened later—in the early Langhian (Otava et al., 2016) by sinistral strike-slip horizontal fault movements (Havíř et al., 2004) forming a canyon-like graben up to 1 km deep (Bubík et al., 2018). The CF, together with the surrounding areas, was subsequently filled and covered with conglomerates, sandstones, and mudstones during the short early Langhian marine transgression

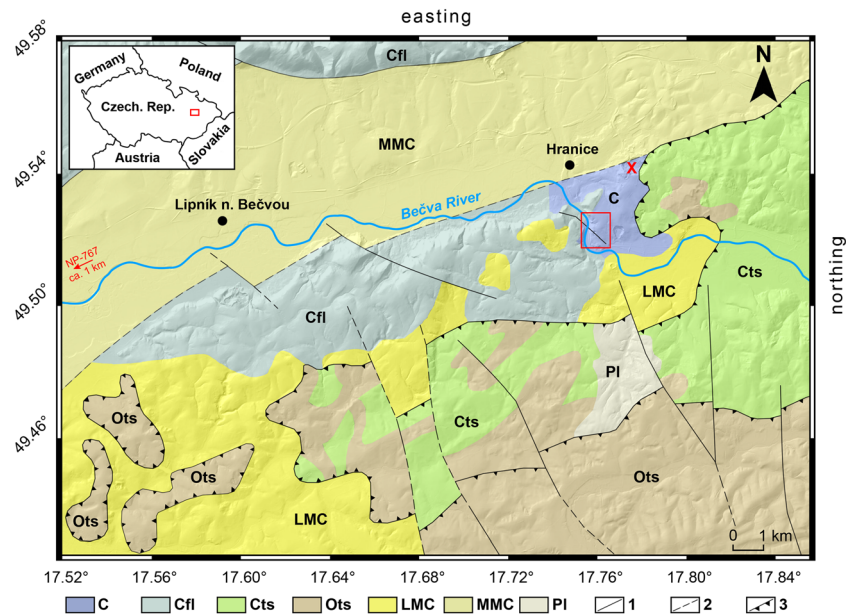


Figure 1. Simplified geological map (compiled after CGS [Czech Geological Survey], 2014, and Otava et al., 2016) with the location of the study area (red rectangle), Skalka limestone quarry (red X), and NP-767 borehole. C, Devonian carbonates; Cfl, Carboniferous flysch deposits; Cts, Cretaceous thrust sheet of the Carpathians; Ots, Oligocene thrust sheet of the Carpathians; LMC, Lower Miocene of the Carpathian Foredeep; MMC, Middle Miocene of the Carpathian Foredeep; PI, Pliocene; 1, faults; 2, suspected faults; 3, thrust terminations.

(e.g., Holcová et al., 2015). These youngest marine sediments were slightly deformed during the final stages of the Alpine Orogeny thrusting (Sracek et al., 2019). Fluvial and lacustrine depositions dominate in following Pliocene and Quaternary periods in the HK and surrounding areas.

The Devonian carbonate sequences within the HK are disrupted by a Variscan deformation foliation (cleavage in 315/40 direction) and NW-SE faults following the prominent regional Elbe Fault Zone direction (Špaček et al., 2015). The younger Alpine Orogeny compression was partly reactivated the Paleozoic NW-SE faults, which opened them to more intense groundwater circulation.

The HK has undergone several periods of limestone dissolution and karst feature formation. The first time carbonates were exposed to a karstification event was during a 3.7 Ma long marine regression at the Frasnian/Famennian transition (Bábek & Novotný, 1999), after which the HK area was exposed to weathering, denudation, and karstification from the early Permian through the early Late Cretaceous (Otava et al., 2009). The karstification stage took place under tropical conditions. The karst weathering formed cavities filled with Cretaceous fluvial clastics of the Rudice Fm. found in cavities exposed in the Skalka limestone quarry (Figure 1; Otava, 2010). The third stage of the karst formation underwent in Cenozoic until the early Miocene when cockpit-like karst morphology was formed at the limestone surface (e.g., Tyráček, 1962). The early Miocene karstification was terminated by a mid-Miocene marine transgression, which covered the whole area with predominantly clastic deposits. The last karstification stage began during the mid-Miocene regression following partial denudation of the marine deposit from the HK surface and continues through to the present. The flooded cave passages are filled with CO₂-enriched water. The high CO₂ content was detected on several groundwater upwelling points concentrated along the SE tectonic border of the CF, both SW and NE of the HK area (Květ & Kačura, 1978).

3. The HA

The dry opening of the HA covers an area of approximately 104 × 34 m with an inclined vertical cavity shape 69.5 m deep with a small lake at the bottom of the chamber. The underwater portion of the HA is an irregular cylinder-like shape with a diameter varying from ~10 to 30 m (Figure 2b). The uppermost 200 m (below water level) of the HA is relatively well documented, compared to the greater depths, which remain poorly

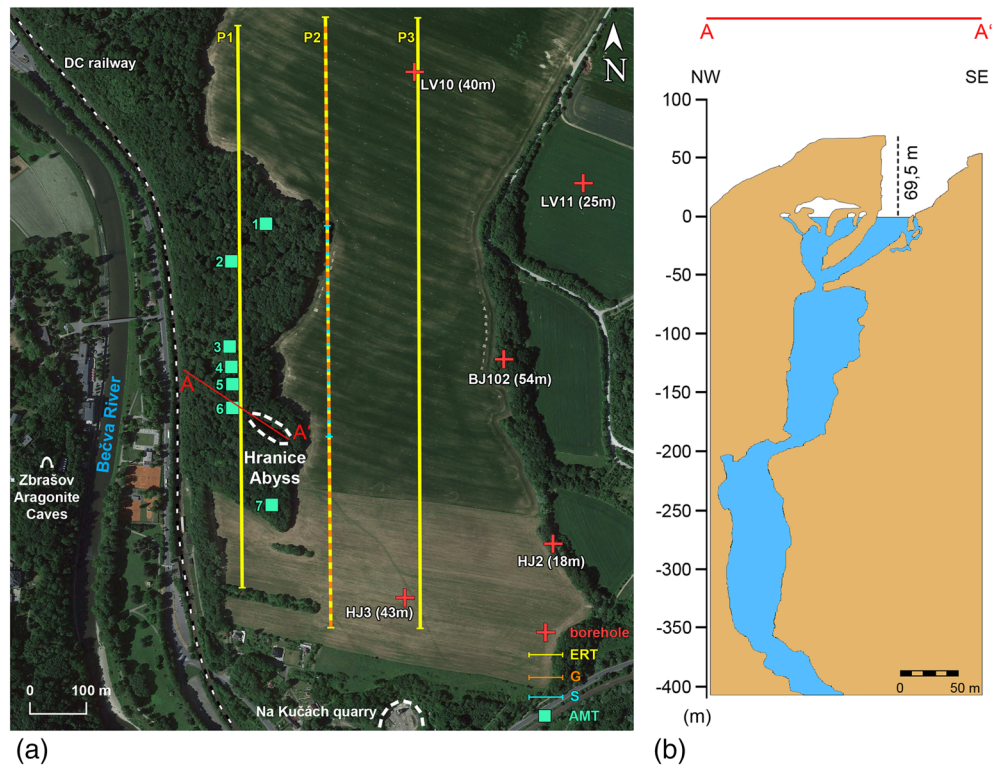


Figure 2. (a) Location of geophysical data collection: ERT, electrical resistivity tomography profiles (P1, P2, P3); AMT, audiomagnetotellurics stations; G, gravity profile; S, seismic measurements; crosses, boreholes with known depth of buried limestone surface. (b) Cross section of the Hranice Abyss along A-A' (see panel (a)). Groundwater table is placed at 0 m and used as reference point (simplified and redrawn after Lukeš, 2018).

understood with limited understanding from ROV and only a few diver's visits by Krzysztof Starnawski (maximum depth -265 m reached 2015) (Zajíček, 2020).

4. Data Acquisition and Processing

Geophysical methods are widely used as a noninvasive tool for imaging the subsurface morphology of karst structures and identification of the thickness and extent of the overlying sedimentary cover. A combination of geophysical techniques including electrical resistivity tomography (ERT), gravity, and seismic methods (e.g., Válois et al., 2011) can be beneficial for characterization of the near-surface structure of karst regions. Information about the deeper structure and morphology requires the use of deeper penetrating techniques such as magnetotellurics (e.g., Hill et al., 2015; Wunderman et al., 2018) and/or using deep-reaching audiomagnetotellurics (AMT) in combination with expanded investigation scales of geophysical methods (resistivity, gravity, and seismic) typically used for near-surface investigations (Blecha et al., 2018).

4.1. Gravity

Gravity measurements were completed using a Scintrex CG-6 gravimeter, with a sensitivity of 0.0001 mGal. The quality of gravity measurements was normally high, with an rms error of 0.005 mGal and repeatability of 0.008 mGal for sites occupied multiple times. The weather during data collection was cold (2 – 5°C), with winds up to 5 m/s and some snowfall. Locations of all gravity points were measured with a GNSS Trimble R10 GPS receiver with a vertical accuracy of 2 cm. A profile of 51 locations with a 20 -m measurement spacing was collected along ERT profile P2 and corrected using a local reference base station.

Gravity data were corrected for instrumental drift, tidal effects, and point elevation. In addition, terrain corrections for distances 0 – $1,000$ m from measured points were calculated using a 0.50 -m (vertical) LiDAR DEM (Digital Elevation Model; CUZK [State Administration of Land Surveying and Cadastre], 2017), while the distal corrections from $1,000$ m to 166.7 km were calculated from the SRTM90 DEM (Jarvis et al., 2008).

Table 1
Density and Porosity Values From Lab Measurements for Two Rock Types
—Limestone (Ls) and Siltstone (Ss)

Rock	Bulk density (kg/m ³)	Grain density (kg/m ³)	Porosity (%)	Wet density (kg/m ³)
Ls 1	2,698	2,712	0.54	2,703
Ls 2	2,702	2,712	0.39	2,706
Ls 3	2,704	2,712	0.27	2,707
Ls 4	2,700	2,711	0.40	2,704
average	2,701	2,712	0.401	2,705
Ls				
Ss 1	2,496	2,676	6.72	2,564
Ss 2	2,542	2,698	5.76	2,600
Ss 3	2,566	2,695	4.80	2,614
Ss 4	2,600	2,734	4.92	2,649
Ss 5	2,535	2,697	6.01	2,595
Ss 6	2,571	2,683	4.17	2,612
Ss 7	2,563	2,708	5.36	2,616
average	2,553	2,699	5.391	2.607
Ss				

Note. The difference is large enough to provide significant contrast for gravity modeling of the limestone topography under siltstone cover.

For the Bouguer correction, a bulk density of 2,670 kg/m³ was used for the near-surface layer of the Earth crust to determine the complete Bouguer gravity anomaly (CBA).

To estimate representative densities for the underlying rock, we collected four samples from a limestone outcrop located ~80 m west of profile P2. The near-surface density was estimated from debris samples (seven samples) along the central part of the profile; these samples are (probably Miocene) siltstone with a medium to fine-grained texture.

Bulk and grain densities of all samples were measured along with porosity and with the wet (fully saturated or “natural”) density calculated from these values. Three weighting methods were used when a sample was measured: (1) dry in the air; (2) in saturation liquid (water); and (3) saturated in the air (details in Carmichael, 1984). The accuracy of the technique is 0.003 kg/m³, and porosity determination is 0.02%. The measured values are presented in Table 1. There is a clear difference between the two rock types (limestones and near-surface rocks) in all parameters except grain density. The most important quantities for the gravity modeling are the wet and bulk density, which, as seen by the laboratory results, have a significant difference between the rock types (e.g., for bulk [dry] density 146 kg/m³ and 98 kg/m³ for wet density).

4.2. Electrical Resistivity Tomography

Three parallel ~1 km north-south ERT profiles were collected using the ARES II resistivity system (GF Instruments, Czechia) with a Wenner-Schlumberger electrode array roughly centered on the HA. Profile P1 has a length of 955 m with an electrode spacing of 5 m, while P2 and P3 both are of length 995 m with a 5-m electrode spacing. The east-west offset between profiles was 150 m (Figure 2a).

4.3. AMT

Seven AMT measurements were collected on a 0.5 km long segment of ERT profile P1. Station spacing for the central portion of the short AMT profile was 30 m with a larger spacing of 150 m for the distal stations. The station layout was based on forward modeling of the expected geometry and extent of the HA. A Metronix ADU06 coil magnetometer system with nonpolarizable electrodes was used for the data acquisition to collect the horizontal components of both the **E** and **H** field; the vertical magnetic field data H_z were not collected. Data quality was hampered by the presence of the nearby DC rail line (130 m from the profile) as well as residential and industrial infrastructure in the area.

The collected data were processed by standard robust techniques (Gamble et al., 1979) using the Mapros implementation (Friedrichs, 2004) with additional notch filtering of noisy frequencies (MathWorks, 2018). The TM mode of the resulting sounding curves are adequate for simple 1-D modeling; unfortunately, the TE mode was heavily affected by the DC noise related to the electric train line and has not been used further in modeling the AMT data set (Pádua et al., 2002).

4.4. Seismic Measurements

Seismic measurements were carried out along the middle portion (~360 m) of profile P2 (Figure 2a). Five 24-channel Geometrics Geode seismographs forming a 120-channel system were coupled with 10- and 20-Hz geophones at 3 m spacing to establish a 357 m long seismic line. A Seismic Impulse Source System (SISSY) was used (GEOSYM GmbH). The SISSY is essentially a buffalo gun with an electrical trigger. The seismic energy provided by its shots is sufficient in typical conditions for investigations of up to ~200 m depth. The seismic wave source spacing along the profile was 12 m (i.e., a four geophone spacing) and included additional offset shots. The length of the seismic record was 2 s, with a sampling period of 125 μs (Figure 3). Obtained seismic data were subsequently processed by seismic tomography and seismic reflection techniques.

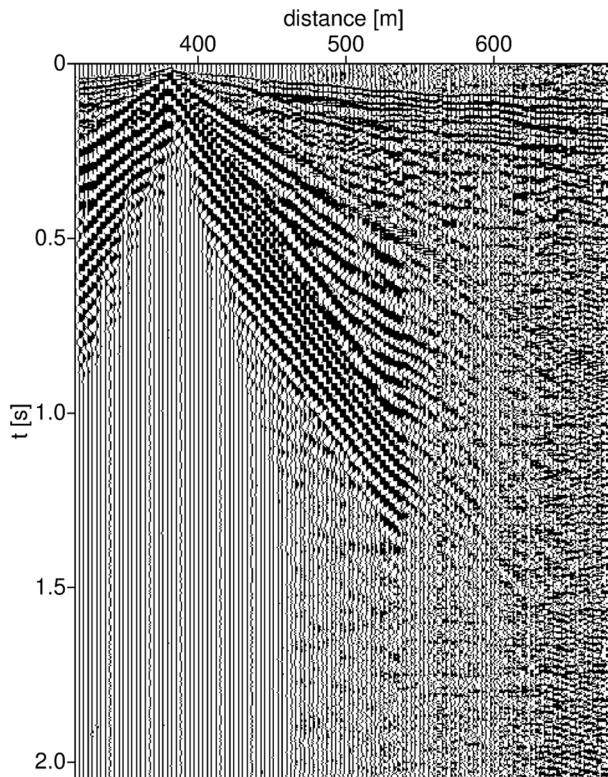


Figure 3. A sample raw shot record (normalized). The first onsets are clearly defined for the distal offsets.

5. Results

5.1. Gravity

The calculated gravity (CBA) curve in Figure 4 rises steeply from the south and then shows two well-distinguished maxima with a minimum between them. The gravity changes along the profile by more than 0.4 mGal, which implies significant changes in density. 2-D modeling of the gravity measurements was undertaken using GM-SYS (GM-SYS Modelling, 2017), incorporating the bulk density values determined from samples collected in this study (bulk density of 2,700 kg/m³ for limestone; 2,500 kg/m³ for sediment overburden; 2,540–2,690 kg/m³ for karstified and weathered zones). Modeling revealed sharp high density “towers” accompanied by less dense blocks forming significant dolines, underlying the low-density surface cover.

5.2. ERT

Data were inverted using the Res2Dinv algorithm (Loke & Barker, 1996), with a topographic correction applied based on the LiDAR DEM (CUZK [State Administration of Land Surveying and Cadastre], 2017; Figure 5). Resistivity values depicted on all three ERT inverted sections (Wenner-Schlumberger array) can be divided into three main features: (i) the low-resistivity (< ~50 Ωm) near-surface layers, (ii) resistivity from 50 to ~400 Ωm with varying thicknesses covering the lowermost layer, and (iii) high to extreme resistivity values (from 400 to thousands of Ωm) in the lowermost layer. All profiles reveal a high-resistivity basement overlain by low-resistivity layers. Profile P1, the closest to the HA, images high-resistivity structures (>1,000 Ωm) above the groundwater level (GWL) parts and lower-resistivity values (<300 Ωm) below the GWL.

The low-resistivity features below GWL are accompanied by a “channel” of lower resistivities (A), which is connected to a significantly lower resistivity zone (<50 Ωm) under the substantial depression in topography (at 450–600 m). Profile P2 shows two resistive units (B and C; >1,000 Ωm) prograding to the surface, which are interrupted by a low-resistivity zone (D; <500 Ωm), while the near-surface layers exhibit low-resistivity values (<50 Ωm). Profile P3 images a low-resistivity layer (<100 Ωm) covering the high-resistivity structure (>1,000 Ωm) along the whole profile.

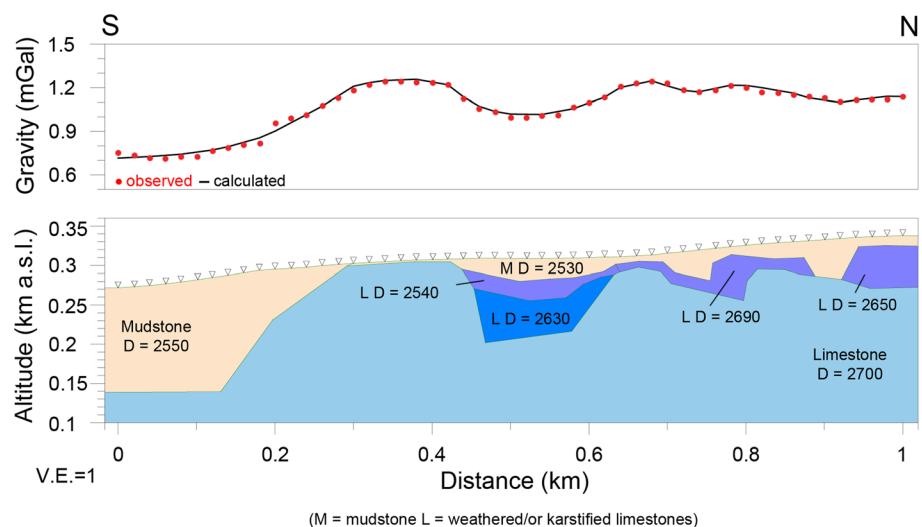


Figure 4. Geological model along the gravity profile with complete Bouguer gravity anomaly. Rock bulk densities are in kg/m³. The root mean square (RMS) error of modeling is 0.017 mGal.

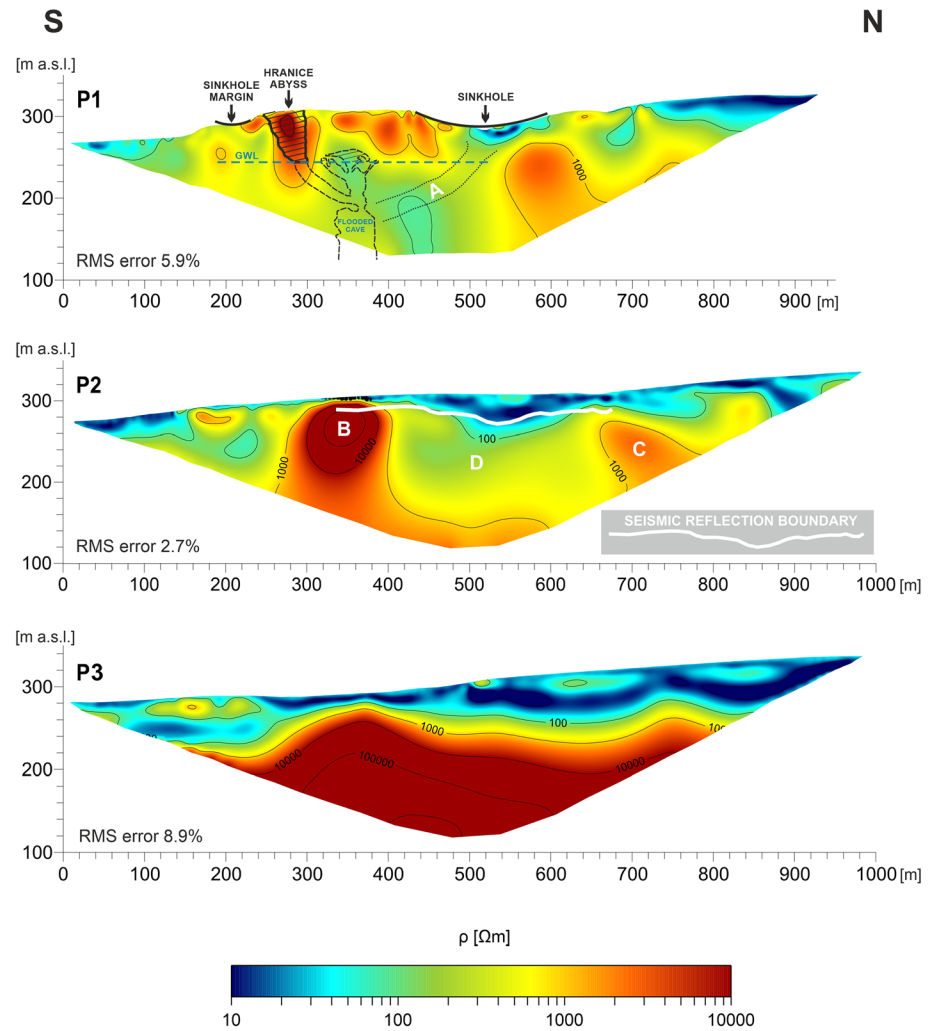


Figure 5. Inversion results for ERT profiles P1 to P3. All three profiles show limestone basement (resistivity > 1,000 Ωm) overlaid by low-resistivity sediments. The most striking feature is the low-resistivity conduit A extending to the surface north of the Hranice Abyss (shape after Guba, 2016). The two high-resistivity units (B and C), together with low-resistivity zone D in the middle of P2, were examined by gravity and seismic surveys.

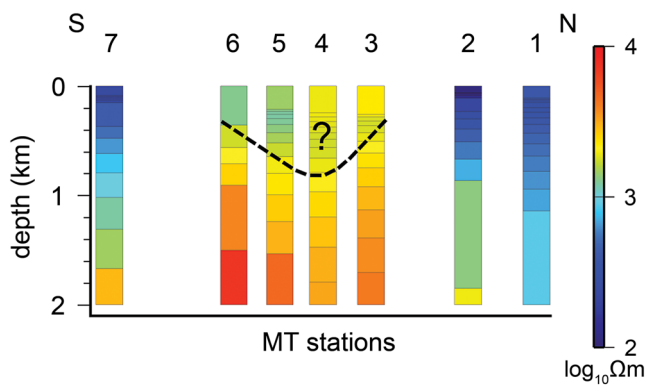


Figure 6. Results of 1-D AMT modeling with marked lower resistivity zone, which could possibly be related to the body of abyss and saturated limestones by mineralized groundwater. The color scale is opposite that of MT standards because it is plotted in the ERT convention.

5.3. AMT

1-D TM (transverse magnetic mode) inversions (Grandis et al., 1999) for each AMT measurement location are shown in Figure 6. The southern extent of the profile is marked by Station 7, which has a near-surface resistivity of ~100 Ωm, increasing to a resistivity of ~1,000 Ωm at a depth of 2 km. The central core of the profile, Stations 3–6, is characterized by near-surface high resistivity (~1,000 Ωm), which extends to ~1 km depth. Below 1 km, the resistivity increases above 10,000 Ωm. The northernmost sites (beyond the HA) are similar to Station 7, again with a low resistivity to ~1 km, underlain by a more resistive (~1,000 Ωm) layer.

5.4. Seismic Measurements

Seismic methods are well suited for distinguishing between the sedimentary rocks which characterize the area of the HA. P wave velocities and seismic reflection coefficients vary significantly for the different sedimentary units.

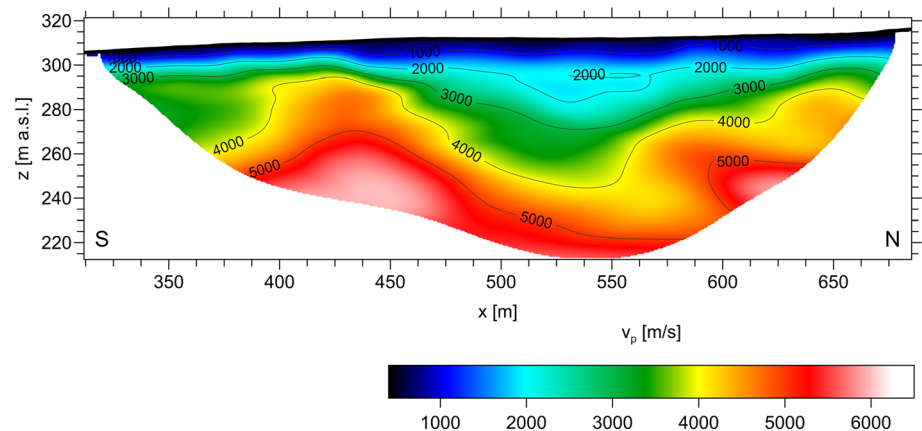


Figure 7. The final tomographical model showing the distribution of P wave velocities. The 3,000-m/s contour line could be considered as a boundary between velocity layers (ii) and (iii).

5.4.1. Seismic Refraction

The V_p seismic tomography model (Figure 7) was determined using the Fresnel volumes approach (Watanabe et al., 1999) as implemented in the Rayfract tomography code (Intelligent Resources Inc.) and had an RMS model fit of 1.20. The starting model used for the inversion was a three-layer model obtained using the plus-minus approach (Hagedoorn, 1959). The V_p section (Figure 7) has a large V_p velocity range, although it is characterized by higher velocities with depth. Four units can be identified in the V_p section: (i) a near horizontal slow layer at the surface ($<1,800$ m/s), (ii) a faster layer (1,800–3,000 m/s) extending to depths of ~ 250 m in the central part of the profile, (iii) a significantly faster layer (3,000–4,000 m/s) underlying layer (ii) that broadly follows its topographic profile, and (iv) the fastest ($>4,000$ m/s) V_p layer underlying the sequence representing the “basement” for the seismic tomography.

5.4.2. Seismic Reflection

Seismic reflection processing was carried out with the ReflexW package (Sandmeier Geophysical Research). The unconsolidated sediments at the surface cause the seismic waves to scatter, hindering wave propagation; as such, the resolution depth for the reflection profile is limited (Figure 8). The reflections appear from the near surface to the depth about 20 m, with the exception between 510 and 580 m, where they are forming U-shaped reflector. No significant reflectors are imaged, which would correspond to deeper structure or layer boundaries.

6. Discussion

Epigenic and hypogenic dissolution represent contrasting formation processes that occur under differing tectonic and hydrologic conditions; as such, the ability to determine which of these are the dominant processes can inform the geologic evolution of the region. In accessible dominantly horizontal cave systems with air-filled passages, features indicative of either epigenic and hypogenic (e.g., sedimentary infill, presence of specific karst features on cave walls, and morphology of passages or different cave patterns) can

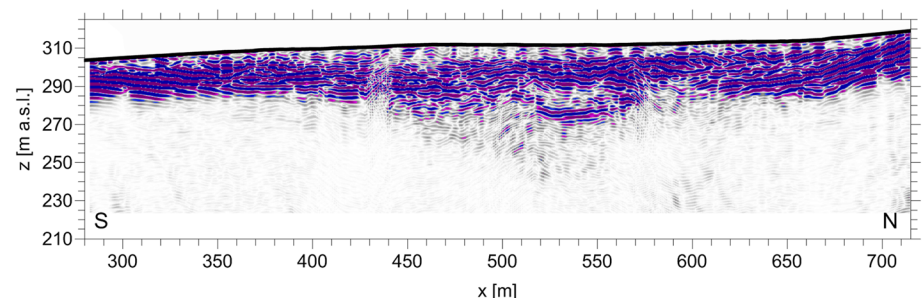


Figure 8. The final stacked and migrated seismic section. The bottommost reflections appear at depths between 20 and 40 m, suggesting a geological boundary.

be found and used to infer formation mechanism (Klimchouk et al., 2016). On the other hand, vertical and subvertical flooded cave systems present a more difficult environment to observe indicative features that reveal the formation mechanism. Historically, indications used to identify formation processes have largely been morphological and relied upon circumstantial evidence such as proximity to faults or basins and the present-day relationship to the surrounding geomorphology and hydrology (Osborne, 2017). Also, determining whether the cave system originated due to hypogenic or epigenic mechanisms is challenging, as descending surface waters may overprint evidence indicative of older hypogenic processes and ascending aggressive late-stage hydrothermal fluids can overprint and erode original structures.

The prevailing consensus for the formation of the HA and similar deep vertical caves elsewhere is hypogenic formation resulting from the presence of deeply sourced CO_2 - and H_2S -bearing temperate waters (e.g., Audra & Palmer, 2015; Auler, 2009; Kunský, 1957). This interpretation is, however, based usually only on present-day observations of temperate waters with particular geochemical composition and lacks the required incorporation of the geological and tectonic evolution of the area during the period of cave formation (Sracek et al., 2019). That is also the case of the HA, where the original idea about the hypogenic speleogenesis (Hynie & Kodym, 1936) is followed to present. The newly discovered presence of a former drainage system in the limestone bedrock with a W/NW orientation together with the local geomorphology at the time of cave formation likely representing a large-scale basin based on tectonic reconstructions of the area suggests a reappraisal of the traditional hypogenic model of cave formation and consideration of cave formation via epigenic processes.

6.1. Geophysical Interpretation

Deep seismic velocity results show elevated velocity ($>3,000$ m/s) typically associated with rigid stronger rock. However, ERT results show a zone of low resistivity corresponding to the zone of elevated seismic velocity; historically, low-resistivity ERT results have been attributed to the presence of fluids or fractures infilled with low-resistivity sediments. Modeling and interpretation of the combined data set must satisfy these seemingly disparate results via the inclusion of constraints from all data types to create a holistic model that fits all data sets to an acceptable level.

The results from different geophysical methods on profile P2 can be interpreted in the framework of a “geophysical stratigraphy.” Seismic refraction results are used to define the geophysical “stratigraphy,” which will be used when discussing the geophysical results from all methods. The topmost layer is represented by unconsolidated Tertiary and Quaternary sediments (Otava et al., 2016) characterized by seismic velocity $<1,800$ m/s with varying thicknesses from surface to ~ 15 m. The base of Layer 1 is identified as the first significant reflector (Figure 8). The ERT identified this layer as a low-resistivity zone with resistivity <50 Ωm .

The second layer consists of marine Miocene sediments (mostly mudstones/sandstones according to borehole evidence) with velocities between 1,800 and 3,000 m/s and varying thickness in depth interval from 10 to 30 m. The basal contact of the layer can be correlated with the second reflection. The ERT did not identify this layer clearly and merged it with the third layer. The gravity modeling based on the seismic and geoelectric results cannot separate the two upper layers and produces a low-density ($2,530$ kg/m^3) zone that represents the top two layers of the geophysical stratigraphy.

The third layer is characterized by seismic velocities of 3,000–4,000 m/s with varying thicknesses in depth interval between 15 and 45 m. It likely represents weathered or cracked limestone, which in the center of the study area is filled by acidic groundwater (ERT profile position 400–640). Reflectors can be identified in the central portion of the profile (position 510–580). The increased thickness of seismic reflections (Figure 8) is in agreement with the lower density ($2,650$ kg/m^3) zone (Figure 4), and they have a resistivity of (50 to ~ 400 Ωm) seen in the ERT as feature “D” (Figure 5).

The lowermost layer corresponds to the rigid limestone basement with velocities exceeding 4,000 m/s and extends to the near-surface in two locations from depth of 20 m to the bottom of the seismic profile (profile position 390–480 and 560–670) marking the two cockpit karst towers. The position of the high-velocity anomalies correlates well with the position of the maxima in the gravity CBA curve and as high resistivity (~ 400 to thousands of Ωm) ERT features “B” and “C” (Figure 5). The lack of reflectors in the layer suggests that this “basement” layer is massive with little internal structure.

Gravity results are questionable on the southern portion of profile P2, where ERT data is limited at depth and seismic reflection was not collected. Modeling of the southern segment of the profile suggests a sedimentary cover thickness up to ~150 m. It is unlikely that the sedimentary cover is actually this thick. An alternate explanation for the gravity minima is void spaces representing unmapped cave structures. Approximately 200 m to the south is the Na Kučách limestone quarry (Figure 2a), where the recently lost entrance to the Černotín caves was discovered in 1866 (Svozilová, 2009). Currently, the entrance to the cave system and the internal structure of the caves is unknown; it is possible that the cave system was destroyed by limestone mining operations. The presence of the gravity low may be explained by void space of the “lost” Černotín cave system, and as such, their destruction during mining is not certain.

The most interesting features are on profile P1, where the HA zone is saturated by acidic mineral water, and thus the HA zone can be tracked vertically to depth. The channel (feature “A” on Figure 5) with lower resistivity corresponds well with the resistivity of the zone interpreted to be saturated with mineral water (the body of the abyss in Figure 5). The channel structure may represent the main crevice of the sinkhole (at 450–600 m), which has a surface expression characterized by a significant topographic depression partly filled with low-resistivity sediments. Given the proximity of the “sinkhole” and the HA, the sinkhole structure can be considered a part of the HA system and may represent the initial stage in the development of a new abyss.

The HA zone is seen on the AMT profile as a north-dipping low-resistivity ($\sim 10^3 \Omega\text{m}$) structure to a depth of ~1 km. The low resistivity is interpreted to represent saturated limestones and coincides with the body of the abyss. The lower resistivity of the AMT section is in agreement with low-resistivity values from ERT, which are unusual for a rigid limestone massif, which would be expected at these depths. The central group of four stations has a common structure, which is interpreted as a single competent block of limestone (or karst tower), in agreement with the interpretation of the ERT results (Figure 5) for this part of the survey area.

In the HA, the water table reaches the void cavity approximately 70 m below the surface, from which the groundwater may be sampled directly. The acidic water sampled in the abyss likely also characterizes the groundwater regime of the karstified and fractured limestones of the survey area (Sracek et al., 2019; Vysoká et al., 2019). The presence of the acidic groundwater is the likely cause for the near-surface low-resistivity zone and its increased depth within the massive limestones on profile P2 (Figure 5, position 400–640).

Cracked or karstified limestones with lower resistivity were also observed by Dleštík and Bábek (2013) and confirmed in nearby boreholes (Fabíková & Peterková, 1963). In both cases, cracks or cavities (caves and caverns) are likely infilled by a significant amount of fine-grained sediments; otherwise, much higher resistivities would be expected if the cracks and cavities were pervasively air-filled voids. However, relatively low resistivity characterizes the limestone bedrock at depths over 100 m (with limestone thickness over 60 m). Intensive karstification to depths of several hundreds of meters is possible (Zajíček, 2017); however, the presence of low-resistivity fine-grain infill at such depths in the massive limestone is questionable.

Figure 9 shows both the present-day (A) surface and the reconstruction of the Devonian limestone basement (B) based on geophysical results. The estimated topology of the reconstructed massive limestone top surface is based on the ERT 1,000 Ωm isoline (and used all three profiles). Comparison of the present and reconstructed limestone surfaces shows that there is significant relief within the limestone bedrock, the topographic highs represent karst towers and the topographic lows dolines.

6.2. New Insight Into the HA Origin

As briefly mentioned above, aside from an older short-lived karstification period in the Late Devonian, significant karst formation in the HK area occurred during the Cretaceous. Large 100 m deep karst sinkhole-like depressions were formed under tropical weathering conditions in the HK, analogous to the Moravian Karst ~75 km SW (see Zajíček, 2017). Relics of these depressions, filled with the Cretaceous Rudice Fm. deposits, were found in the Skalka limestone quarry (Otava et al., 2016). These tropical karst features have been markedly eroded due to Paleogene weathering and denudation processes (Špaček et al., 2015).

The Alpine Orogeny and the nappe thrusting event induced regional compression during the early Miocene at the contact of the Bohemian Massif and Carpathian orogenic belt (Špaček et al., 2015). In the nappe

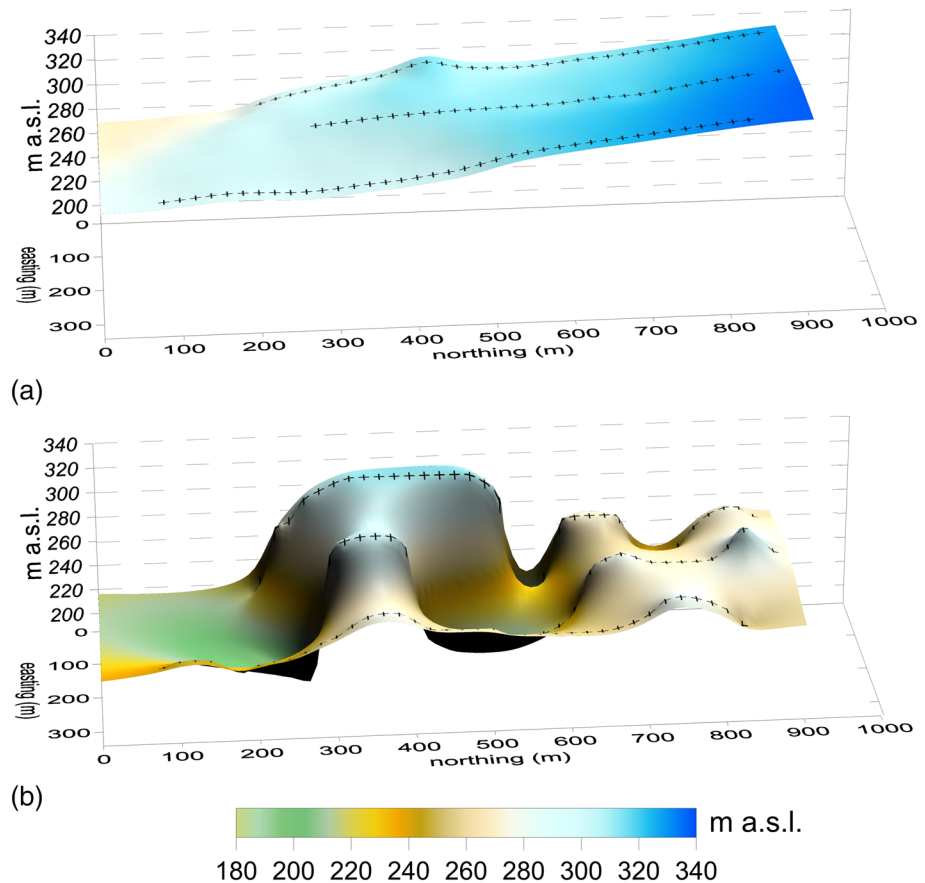


Figure 9. Recent surface (a) compared to a probable rigid limestone surface (b) reconstructed on the 1,000 Ωm contour line from all three ERT profiles. Crosses mark points where the 1,000 Ωm isoline was present.

foreland, a 900-m deep graben opened proximal to the HK (Bubík & Otava, 2016). The canyon-like graben opened in the early Langhian (Otava et al., 2016) from horizontal sinistral strike-slip movement (pull-apart mechanism) along the NE-SW faults induced by the regional compression (Havíř et al., 2004). The horizontal movements and deformations are recorded in the paleomagnetic rotations of early Langhian marine deposits filling the CF graben (Márton et al., 2011). The fast CF opening triggered intense regional erosion leading to the formation of river valleys, pointing to the CF basin and deeply incised the eastern margin of the Bohemian Massif (Dvořák & Slezák, 1953). Borehole logging shows these incised valleys often follow the NW-SE faults and could be up to 300 m deep. One such buried early Miocene valley is located on the opposite side of the CF, approximately 15 km NNW of the HK area (Nehyba et al., 2019). Its hanging position with respect to the 900-m depth of the CF indicates two stages of CF graben opening. During the subsequent early Langhian marine transgression, the CF, together with these hanging valleys, was filled with marine sandstones and claystones (Bubík et al., 2018).

The Prosenice borehole, located 20 km SW of the HA, reached the limestone basement beneath the CF at a depth of 897.2 m below surface (Huřová, 1974)—that is, -682.2 m a.s.l. The 900-m deep CF was a local erosional base for both surface and subsurface waters running across the HK carbonates during the early Miocene. Paleozoic limestone bedding and deformation cleavage dip steeply (up to 40°) to the NW—that is, toward the CF (Havíř et al., 2004). The dip of the limestone beds implies a continuation of the carbonate sequences, underlying the nonkarstic deposits, toward the base of the CF (see Figure 10).

The early Miocene karst surface morphology, reconstructed from borehole data, shows valleys and dolines with E-W and SW-NE orientations, which have been, eroded by westward running surface waters—that is, toward the CF (Otava, 2006). Additionally, running surface waters formed the cockpit-like features, which characterize the karst surface (Kodym, 1960; Tyráček, 1962). The presence of early Langhian

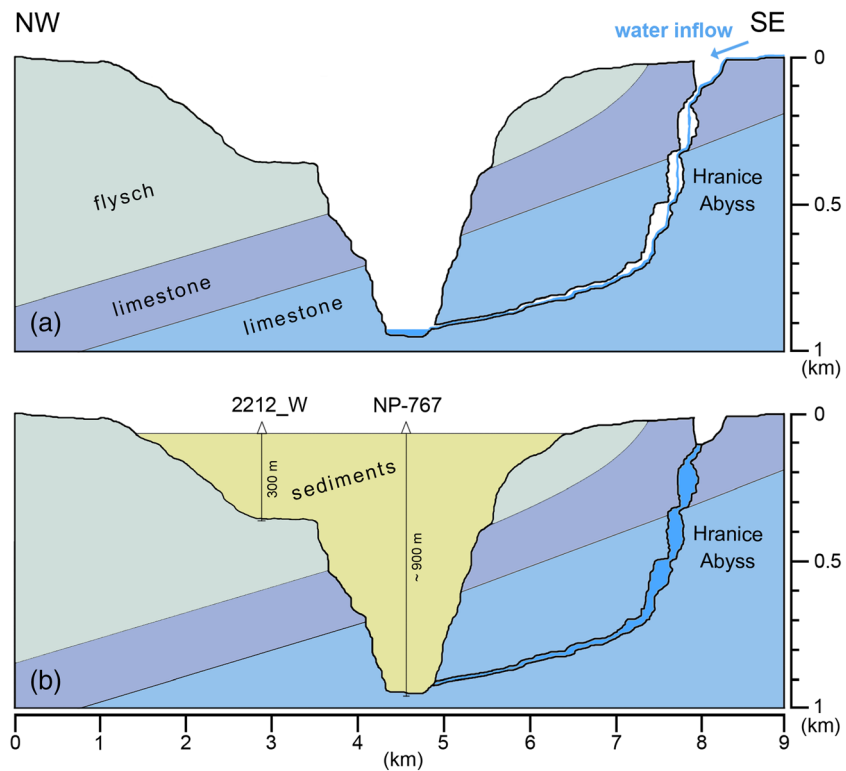


Figure 10. Conceptual geological cross section through the Hranice Abyss and Carpathian Foredeep. Panel (a) shows the situation during early Langhian, when CF was opened and the HA originated, while panel (b) displays current state with known boreholes. 3.5X vertically exaggerated.

marine deposits infilling cavities in the HA walls above the modern water table extent of the cave system (i.e., above the flooded portion) can also be observed in the Zbrašov Aragonite Caves (ZAC) (Otava, 2006, 2016; Sracek et al., 2019), suggesting vertical excavation from descending surface water.

Based on the geological, structural, and geomorphological evidence found in the HK area and its close surroundings, we propose the HA originated by erosion processes of surface waters descending from the karst surface and running underground to the local erosional base, which marks the bottom of the 2–3 km distant CF (Figure 10). The epigenic vadose water circulation regime should dominate during the HA formation. Local structural elements were the dominant control during limestone dissolution and cavity formation. The HA developed at an intersection of dislocation thrusting parallel to cleavage and the subvertical NW-SE faulting (Otava, 2010; Sracek et al., 2019), making the area preferentially susceptible to vertical water circulation. The HA depth is limited by the depth of the local erosional base, that is, by the CF depth ~900 m; as such, the maximum depth of the HA is inferred to be between 800 and 1,000 m, which can be seen in the AMT results (Figure 6).

Following the mid-Miocene marine transgression and widespread deposition of clastic sediments, including the HK, active karst processes were interrupted. The original late-early Miocene cave springs, which originally outflowed at the base of the CF, including the HA spring, were choked by the marine deposits filling the CF graben. The choking or blocking of these springs at the base of the karst zone forced a rise of the water table from pre- to mid-Miocene levels (~800–1,000 m below the surface) to the current level ~70 m below surface. The rise in the water table depth resulted in flooding of much of the extent of the HA, the deeper levels of the ZAC, and causing upwelling in springs at the Bečva River valley bottom (Vysoká et al., 2019). The upwelling waters are CO₂ enriched and use existing “crustal-structural soft zones” in their ascent via faults and tectonic cleavage. A high concentration of ²²⁶Ra dissolved in the mineral water indicates that the groundwater is in contact with the crystalline complexes underlying the carbonate sequences (Švajner, 1982). Limestone dissolution by these temperate mineral waters continues to modify the HA resulting in its current extent (Kodym 1960; Kinský, 1957). The HK region, including the early Miocene development

of the HA structure, formed via dominantly epigenic processes (Kodym, 1960; Tyráček, 1962) with later secondary evolution and overprinting of the original cavities by hypogenic processes (see Geršl & Šimečková, 2009).

The novel interpretation of an epigenic formation model for the HA is analogous to that used to explain the formation of the Fontaine de Vaucluse flooded caves (Audra et al., 2004). In both cases, local erosional base deepening and canyon-like depression forming are crucial in the cave's evolution. However, different mechanisms are proposed for canyon formation; the HA canyon-like graben was opened by extensional strike-slip horizontal movement (Havíř et al., 2004), while the Fontaine de Vaucluse canyon was incised due to the Mediterranean Sea low-stand during the Messinian period (Audra et al., 2004). In both cases, the canyon formations were followed by the development of deep epigenic cave systems formed by surface waters, which resurged at the canyon base. Subsequent sediment deposition (via sea-level rise) and infill of these canyons caused spring outflows to become blocked and the cave systems to be flooded with fresh water.

6.3. Implications for the Origin of Other Deep Vertical Caves

The updated model for the formation of the HA demonstrates the benefit of inclusion of new lines of investigation (in this case, multiple geophysical data sets). The inclusion of geophysical results provided new insight into the geological and morphological history of the HA karst. This approach can lead to further understanding of similar karst evolution and formation for deep flooded cave systems elsewhere. Large-scale cave formation is, of course, dependent on water flux; the nature and direction of that water movement are controlled by the tectonic conditions at the time of cave formation which can be inferred from former drainage patterns, groundwater saturated zones, or evidence of variations in local/regional erosional base.

However, the clear evidence for hypogenic cave evolution—for example, unusual groundwater mineralization (Farrant & Harrison, 2017), presence of artesian aquifers and preferably oriented faults (Klimchouk et al., 2017), or the occurrence of characteristic karst features (cupolas and uncommon speleothems) (Gázquez et al., 2017)—is often missing in giant shafts. The lack of detailed information and difficulty in making direct observations in deep flooded cave systems make the inclusion of geophysical surveys a necessity when investigating the processes responsible for large-scale karst cave formation.

Detailed multidisciplinary studies of the world's deepest flooded cave systems and their associated formation mechanisms are rare. A hypogenic origin is suggested for the Pozzo del Merro and Zacatón systems based on the nearby presence of volcanic bodies (Gary, 2017; Gary et al., 2003). The present-day warm mineral waters are also used to infer the hypogenic evolution of the Lagoa Misteriosa cave system in Brasilia (Auler, 2009). Multiple epigenic formation models have been presented for the Red Lake formation in Croatia, variously suggesting that it is a collapsed doline or sinkhole; all of these formation models are based on geologic and hydrologic evidence alone (Andrić & Bonacci, 2014; Bahun, 1991; Petrik, 1960; Williams, 2004). Geophysical imaging of these systems could reveal important new evidence of the geologic evolution and formation processes of these systems.

7. Conclusion

Understanding the evolutionary history of deep-flooded caves is difficult given the challenges with making direct observations of these systems. The traditionally accepted hypogenic formation of these systems is largely based on the occurrence of present-day temperate water containing acidic elements originating from a deep source. Based on newly acquired geophysical data sets in the area surrounding the HA, a reappraisal of the accepted hypogenic origin of the system indicates, rather, that epigenic (top-down) processes were dominant during the formation of the large-scale karst system. However, the current secondary evolution of the system is dominated by hydrothermally driven hypogenic (bottom-up) processes. In the preferred top-down formation process, water would have run underground toward the local basal erosional surface—the bottom of the CF—before the mid-Miocene marine transgression event. The ERT results indicate the presence of a “fossil” sediment-filled sinkhole connected to the main vertical shaft of the HA cave system. The connection of the “fossil” sinkhole to the HA indicates a larger spatial extent of the karstified dislocation zone - a first-order control on the origin and morphology of the HA. The inclusion of geophysical results enabled a complete consideration of the formation model by revealing key information about the geological and

morphological evolution of the system, which was then used in conjunction with tectonic and geologic evidence to construct a consistent formation model. This approach is readily applicable to similar flooded cave systems globally.

Data Availability Statement

All geophysical data presented here are available in standard industry formats from <https://doi.org/10.17632/fjkbpb2gd.1>.

Acknowledgments

The research was cofunded by the institutional support of the Center for Geosphere Dynamics (UNCE/SCI/006), by the support of the long-term conceptual development research organization RVO: 67985891, and by Operational Program VVV CZ.02.1.01/0.0/0.0/16_013/0001800. Special thanks to Helena Vysoká for help with the preparation of the measurements and accessing the locality. Thanks to Filip Hartvich for help with ERT measurements and Václav Polák with gravity survey.

References

- Ardrić, I., & Bonacci, O. (2014). Morphological study of Red Lake in Dinaric karst based on terrestrial laser scanning and sonar systems. *Acta Carsologica*, 43(2–3), 229–239. <https://doi.org/10.3986/ac.v43i2.712>
- Audra, P., Mocočian, L., Camus, H., Gilli, É., Clauzon, G., & Bigot, J.-Y. (2004). The effect of the Messinian Deep Stage on karst development around the Mediterranean Sea. Examples from southern France. *Geodinamica Acta*, 17(6), 389–400. <https://doi.org/10.3166/ga.17.389-400>
- Audra, P., & Palmer, A. N. (2015). Research frontiers in speleogenesis. Dominant processes, hydrogeological conditions and resulting cave patterns. *Acta Carsologica*, 44(3), 315–348. <https://doi.org/10.3986/ac.v44i3.1960>
- Auler, A. S. (2009). Styles of hypogene cave development in ancient carbonate areas overlying non-permeable rocks in Brazil and the influence of competing mechanisms and later modifying processes. In A. Klimchouk & D. Ford (Eds.), *Hypogene speleogenesis and karst hydrogeology of artesian basins* (pp. 173–180). Simferopol: Ukrainian Institute of Speleology and Karstology.
- Bábek, O., & Novotný, R. (1999). The Hněvotín Limestone neostratotype locality revisited: A Conodont biostratigraphy and carbonate microfacies approach, Moravia, Czech Republic. *Acta Univ. Pal. Olom. Fac. Rer. Natural., Geologica*, 36, 63–68.
- Bahun, S. (1991). O postanku Crvenog i Modrog jezera kod Imotskog (Genesis of Red and Blue Lakes near Imotski). *Geoloski Vjesnik*, 44, 275–280.
- Blecha, V., Fischer, T., Tábořík, P., Vilhem, J., Klanica, R., Valenta, J., & Štěpančíková, P. (2018). Geophysical evidence of the eastern marginal fault of the Cheb basin (Czech Republic). *Studia Geophysica et Geodaetica*, 62(4), 660–680. <https://doi.org/10.1007/s11200-017-0452-9>
- Bubík, M., Břizová, E., Buriánek, D., Gilíková, H., Havří, J., Janderková, J., et al. (2018). *Explanatory notes to the basic geological map of Czech. Rep., sheet Lipník nad Bečvou 25-132* (pp. 1–185). Czech Geological Survey Archive (in Czech).
- Bubík, M., Otava, J. (2016). Geologický vývoj. In J. Otava, O. Bábek, M. Bubík, D. Buriánek, J. Čurda, J. Franců, et al. (Eds.), *Explanatory notes to the basic geological map of Czech. Rep., sheet Kelč 25-141* (pp. 1–115). Czech Geological Survey (in Czech).
- Carmichael, R. S. (1984). *CRC handbook of physical properties of rocks* (Vol. III, p. 354). New York: CRC Press Inc.
- Carvalho, J., Matias, H., Torres, L., Manupella, G., Pereira, R., & Mendes-Victor, L. (2005). The structural and sedimentary evolution of the Arruda and Lower Tagus sub-basins, Portugal. *Marine and Petroleum Geology*, 22(3), 427–453. <https://doi.org/10.1016/j.marpetgeo.2004.11.004>
- CGS (Czech Geological Survey) (2014). Geological map of the Czech Republic 1:500 000. Internet application, available from <https://mapy.geology.cz/geocr500/>
- CUZK (State Administration of Land Surveying and Cadastre) (2017). Digital terrain model of the Czech Republic of the 5th generation (DMR 5G), [https://geoportal.cuzk.cz/\(S\(isdmsblejuka31kelctuwjij\)\)/Default.aspx?lng=EN&mode=TextMeta&side=vyskopis&metadataID=CZ-CUZK-DMR5G-V&head](https://geoportal.cuzk.cz/(S(isdmsblejuka31kelctuwjij))/Default.aspx?lng=EN&mode=TextMeta&side=vyskopis&metadataID=CZ-CUZK-DMR5G-V&head)
- Dleštík, P., & Bábek, O. (2013). *Shallow geophysical mapping of buried karst surface near Hranice using electrical resistivity tomography, Geologické výzkumy na Moravě a ve Slezsku*, 20 (pp. 1–2) (in Czech). Available at <https://journals.muni.cz/gvms/article/view/1568>
- DuChene, H. R., Palmer, A. N., Palmer, M. V., Queen, J. M., Polyak, V. J., Decker, D. D., et al. (2017). Hypogene speleogenesis in the Guadalupe Mountains, New Mexico and Texas, USA. In A. Klimchouk, A. N. Palmer, J. de Waele, A. S. Auler, & P. Audra (Eds.), *Hypogene karst regions and caves of the world* (pp. 511–530). New York: Springer International Publishing.
- Dvořák, J., & Slezák, L. (1953). *Caves in the area of the Hranice devonian*. *Čs. kras* (Vol. VI, pp. 175–184). Brno (in Czech).
- Fabíková & Peterková (1963). Borehole profiles HJ-1/2/3. In *Hydrogeological survey report from Čertotín, Czech Geological Survey—Geofond Archive* (in Czech).
- Farrant, A. R., & Harrison, T. (2017). Hypogenic caves in UK. In A. Klimchouk, A. N. Palmer, J. de Waele, A. S. Auler, & P. Audra (Eds.), *Hypogene karst regions and caves of the world* (pp. 43–60). New York: Springer International Publishing.
- Ford, D. C., & Williams, P. (2007). *Karst hydrogeology and geomorphology* (p. 562). New York: John Wiley & Sons Inc. <https://doi.org/10.1002/9781118684986>
- Friedrichs, B. (2004). *Mapros (Ver. 0.87b freeware)*.
- Gamble, T. D., Goubau, W. M., & Clarke, J. (1979). Magnetotellurics with a remote magnetic reference. *Geophysics*, 44(1), 53–68. <https://doi.org/10.1190/1.1440923>
- Gary, M. O. (2017). Sistema Zacatón: Volcanically controlled hypogenic karst, Tamaulipas, Mexico. In A. Klimchouk, A. N. Palmer, J. de Waele, A. S. Auler, & P. Audra (Eds.), *Hypogene karst regions and caves of the world* (pp. 769–782). New York: Springer International Publishing.
- Gary, M. O., Sharp, J. M. Jr, Caramana, G., & Havens, R. H. (2003). *Volcanically influenced speleogenesis: Forming El Sistema Zacatón, Mexico, and Pozzo Merro, Italy, the deepest phreatic sinkholes in the world*. Geological Society of America.
- Gázquez, F., Calaforra, J. M., Estrella, T. R., Ros, A., Llamusi, J. L., & Sánchez, J. (2017). Evidence for regional hypogene speleogenesis in Murcia (SE Spain). In A. Klimchouk, A. N. Palmer, J. de Waele, A. S. Auler, & P. Audra (Eds.), *Hypogene karst regions and caves of the world* (pp. 85–98). New York: Springer International Publishing.
- Geršl, M., & Šimečková, B. (2009). Zbrašov aragonite caves, Hranice abyss. In J. Hromas, Caves, P. Mackovčín, & M. Sedláček (Eds.), *Protected areas of Czechia, sv. XIV., AOPK Praha* (pp. 363–368).
- GM-SYS Modelling (2017). <http://www.geosoft.com/products/gm-sys>
- Grandis, H., Menvielle, M., & Roussignol, M. (1999). Bayesian inversion with Markov chains—I. The magnetotelluric one-dimensional case. *Geophysical Journal International*, 138(3), 757–768. <https://doi.org/10.1046/j.1365-246x.1999.00904.x>

- Guba, M. (2016). *A press release for the depth survey of the Hranice Abyss and reaching a new maximum depth –404 m* (in Czech). Retrieved from <http://www.hranickapropast.cz/>
- Hagedoorn, J. G. (1959). The plus-minus method of interpreting seismic refraction sections. *Geophysical Prospecting*, 7(2), 158–182. <https://doi.org/10.1111/j.1365-2478.1959.tb01460.x>
- Haviř, J., Krejčí, O., & Otava, J. (2004). Tektonika. In J. Otava, J. Adámek, M. Adamová, O. Bábek, E. Brízová, M. Bubík, et al. (Eds.), *Explanatory notes to geological map 1:25 000 Hranice 25–123*. Czech Geological Survey (in Czech).
- Hill, G. J., Bibby, H. M., Ogawa, Y., Wallin, E. L., Bennie, S. L., Caldwell, T. G., et al. (2015). Structure of the Tongariro volcanic system: Insights from magnetotelluric imaging. *Earth and Planetary Science Letters*, 432, 115–125. <https://doi.org/10.1016/j.epsl.2015.10.003>
- Holcová, K., Hrabovský, J., Nehyba, S., Hladilová, Š., Doláková, N., & Demény, A. (2015). The Langhian (Middle Badenian) carbonate production event in the Moravian part of the Carpathian Foredeep (central Paratethys): A multiproxy record. *Facies*, 61(1), 419. <https://doi.org/10.1007/s10347-014-0419-z>
- Hufová, E. (1974). *Radslavice NP 767. Final report* (pp. 1–177). Czech Geological Survey (in Czech).
- Hynie, O., & Kodým, O. (1936). *Mineral water springs in the Teplice nad Bečvou Spa: Reconstruction of water abstraction in years 1932–1934* (Vol. 11, pp. 61–117). Sborník SGÚ (in Czech).
- Jarvis, A., Reuter, H. I., Nelson, A., & Guevara, E. (2008). Hole-filled SRTM for the globe version 4. In *CGIAR-CSI SRTM 90m database*. Available at <http://srtm.csi.cgiar.org>
- Kalvoda, J., Bábek, O., Fatka, O., Leichmann, J., Melichar, R., Nehyba, S., & Spacek, P. (2008). Brunovistulian terrane (Bohemian Massif, Central Europe) from late Proterozoic to late Paleozoic: A review. *International Journal of Earth Sciences*, 97(3), 497–518. <https://doi.org/10.1007/s00531-007-0183-1>
- Klimchouk, A., Auler, A. S., Bezerra, F. H. R., Cazarin, C. L., Balsamo, F., & Dublyansky, Y. (2016). Hypogenic origin, geologic controls and functional organization of a giant cave system in Precambrian carbonates, Brazil. *Geomorphology*, 253, 385–405. <http://doi.org/10.1016/j.geomorph.2015.11.002>
- Klimchouk, A., Palmer, A. N., de Waele, J., Auler, A. S., & Audra, P. (2017). *Hypogene karst regions and caves of the world* (p. 911). New York: Springer International Publishing. <https://doi.org/10.1007/978-3-319-53348-3>
- Kunský, J. (1957). Thermomineral karst and caves of Zbrašov, Northern Moravia. *Sbor. Čs. spol.zeměp.*, sv. 62/1957, 306–351 (in Czech).
- Květ, R., & Kačura, G. (1978). *Mineral waters of the northern Moravia region* (pp. 1–173). Praha: Ústř. Úst. Geol.
- Loke, M. H., & Barker, R. D. (1996). Rapid least-squares inversion of apparent resistivity pseudosections using a quasi-Newton method. *Geophysical Prospecting*, 44(1), 131–152. <https://doi.org/10.1111/j.1365-2478.1996.tb00142.x>
- Lukeš, J. (2018). *The Hranice Abyss, schematic map, state at 1.1.2017*. Retrieved from <http://hranickapropast.cz/mapy/>
- Márton, E., Tokarski, A., Krejčí, O., Rauch, M., Olszewska, B., Tomanová Petrová, P., & Wójcik, A. (2011). Non-Europea palaeomagnetic directions from the Carpathian Foredeep at the southern margin of the European plate. *Terra Nova*, 23, 134–144. <https://doi.org/10.1111/j.1365-3121.2011.00993.x>
- MathWorks (2018). Signal Processing Toolbox: User's Guide (R2018a). https://www.mathworks.com/help/pdf_doc/signal/signal_tb.pdf
- Meyberg, M., & Rinne, B. (1995). *Messung des 3He/4He-Isotopenverhältnisses im Hranicka Propast (Tschechische Republik)* (Vol. 46, No. 1, pp. 5–8). Wien: Die Höhle, Zeitschrift für Karst- und Höhlenkunde.
- Nehyba, S., Gilíková, H., Tomanová Petrová, P., Otava, J., & Skácelová, Z. (2019). Evolution of a sedimentary infill of a palaeovalley at a distal margin of the peripheral foreland basin. *Geological Quarterly*, 63(2), 319–344. <https://doi.org/10.7306/gq.1469>
- Osborne, R. A. L. (2017). Hypogene caves of the Tasmanic Karsts of eastern mainland Australia. In A. Klimchouk, A. N. Palmer, J. de Waele, A. S. Auler, & P. Audra (Eds.), *Hypogene karst regions and caves of the world* (pp. 893–911). New York: Springer International Publishing.
- Otava, J. (2006). Current state of knowledge of polyphase karstification of the Hranice Paleozoic. *Speleofórum 2006*, s. 84–86, Praha (in Czech).
- Otava, J. (2010). Geological guide of Hranice area or when the orogenes collides. *Česká geologická společnost*, 28 s., Praha (in Czech).
- Otava, J. (2016). Geologically significant sites. In Otava, J., Bábek, O., Bubík, M., Buriánek, D., Čurda, J., Franců, J. et al. (2016). Explanatory notes to the basic geological map of Czech. Rep., sheet Kelč 25–141. Czech Geological Survey, 115p (in Czech).
- Otava, J., Bábek, O., Bubík, M., Buriánek, D., Čurda, J., Franců, J. et al. (2016). Explanatory notes to the basic geological map of Czech. Rep., sheet Kelč 25–141. Czech Geological Survey, 115p (in Czech).
- Otava, J., Geršl, M., Haviř, J., Bábek, O., & Kosina, M. (2009). The Hranice Abyss—Through the eyes of geologists, *Ochrana přírody*, roč. 64, 1, s. 18–22., Praha (in Czech).
- Pádua, M. B., Padilha, A. L., & Vitorello, Í. (2002). Disturbances on magnetotelluric data due to DC electrified railway: A case study from southeastern Brazil. *Earth, Planets and Space*, 54(5), 591–596. <https://doi.org/10.1186/BF03353047>
- Petrik, M. (1960). Hidrografská mjerenja u okolici Imotskog (Hydrographic measurements near Imotski). *Ljetopis JAZU*, 64, 266–286.
- Šmejkal, V., Hladilová, J., Pfeiferová, A., & Melková, J. (1976). Isotopic composition of carbon and oxygen in speleothems from karst caves in northern Moravia. In: J. Čadek & Pačes T (Eds.), *Proceedings of International Symposium on Water-Rock Interaction, Czechoslovakia 1974*: 363–367. Praha.
- Špaček, P., Bábek, O., Štěpánčíková, P., Švancara, J., Pazdírková, J., & Sedláček, J. (2015). The Nysa-Morava zone: An active tectonic domain with Late Cenozoic sedimentary grabens in the Western Carpathians' foreland (NE Bohemian Massif). *International Journal of Earth Sciences*, 104(4), 963–990. <https://doi.org/10.1007/s00531-014-1121-7>
- Sracek, O., Geršl, M., Faimon, J., & Bábek, O. (2019). The geochemistry and origin of fluids in the carbonate structure of the Hranice Karst with the world's deepest flooded cave of the Hranicka Abyss, Czech Republic. *Applied Geochemistry*, 100, 203–212. <https://doi.org/10.1016/j.apgeochem.2018.11.013>
- St. Kodým, O. (1960). About the Hranice Karst genesis. *Čas. Min. Geol.*, 5(3), 262–264 (in Czech).
- Švajner, L. (1982). *Hydrogeology of mineral waters in Teplice above Bečva R.* (Diploma thesis). Bratislava, Slovakia: Komenský University.
- Svozilová, M. (2009). The characteristic of karst processes and landforms in the Hranický Kras Area (Handbook for teachers of geography) (Bachelor thesis). Palacký University Olomouc (in Czech).
- Tyráček, J. (1962). Fossil cockpit karst near Hranice na Moravě. *Časopis pro Mineral. A Geol.*, 2, s. 176–185 (in Czech).
- Válois, R., Camerlynck, C., Dhemaied, A., Guerin, R., Hovhannissian, G., Plagnes, V., et al. (2011). Assessment of doline geometry using geophysics on the Quercy plateau karst (South France). *Earth Surface Processes and Landforms*, 36(9), 1183–1192. <https://doi.org/10.1002/esp.2144>
- Vysoká, H., Bruthans, J., Falteisek, L., Žák, K., Rukavičková, L., Holeček, J., et al. (2019). Hydrogeology of the Hranice abyss (Czechia)—The deepest underwater cave in the world. *Hydrogeology Journal*, 27(7), 2325–2345. <https://doi.org/10.1007/s10040-019-01999-w>

- Watanabe, T., Matsuoka, T., & Ashida, Y. (1999). Seismic traveltime tomography using Fresnel volume approach. SEG Technical Program Expanded Abstracts 18. <https://doi.org/10.1190/1.1820777>
- Williams, P. (2004). Dolines. In J. Gunn (Ed.), *Encyclopedia of caves and karst science* (pp. 628–642). London, UK: Fitzroy Dearborn.
- Wunderman, R. L., Wannamaker, P. E., & Young, C. T. (2018). Architecture of the hidden Penokean terrane suture and midcontinent rift system overprint in eastern Minnesota and western Wisconsin from magnetotelluric profiling. *Lithosphere*, *10*(2), 291–300. <https://doi.org/10.1130/L716.1>
- Zajíček, P. (2017). The Moravín karst in submersible river of time. *Academia*, 276p (in Czech).
- Zajíček, P. (2020). Karst areas of the middle and northern Moravia and Silesia. *Academia*, 246p (in Czech).
- Zhou, W., Beck, F. B., & Adams, A. L. (2002). Effective electrode array in mapping karst hazards in electrical resistivity tomography. *Environmental Geology*, *42*(8), 922–928. <https://doi.org/10.1007/s00254-002-0594-z>